

NUMERICAL ANALYSIS OF WAVEFIELDS IN COMPOSITE FROZEN POROUS MEDIA

Claudia L. Ravazzoli^a, Germán Rubino^a and Juan E. Santos^{a,b}

^a Facultad de Ciencias Astronómicas y Geofísicas, Universidad Nacional de La Plata,
Paseo del Bosque s/n, 1900 - La Plata, Argentina and CONICET
e-mail: claudia@fcaglp.fcaglp.unlp.edu.ar,
grubino@fcaglp.fcaglp.unlp.edu.ar

^b Facultad de Ciencias Astronómicas y Geofísicas, Universidad Nacional de La Plata,
Paseo del Bosque s/n, 1900 - La Plata, Argentina and CONICET
Also Department of Mathematics, Purdue University,
W. Lafayette, IN, 47907, USA.
e-mail: santos@fcaglp.fcaglp.unlp.edu.ar

Key Words: porous media, numerical simulation, wave propagation, composite solids.

Abstract.

Using a physical model presented by some of the authors in previous works, we analyze the propagation of elastic waves in multiphase porous media composed by two weakly coupled solids, saturated by a viscous single-phase fluid. The model predicts the existence of three compressional and two shear modes of propagation. The set of partial differential equation is solved using an iterative domain decomposition finite element procedure in the space-frequency domain, which allows us to include the frequency dependence of dissipation, mass and viscous coupling coefficients in the high frequency range.

We focus the attention in the numerical simulation of ultrasonic wave generation and propagation in a small sample of a partially frozen sandstone (permafrost) with non-uniform water-ice distribution, to analyze the correlation between the heterogeneities, scattering and wave mode conversion effects taking place under these conditions.

1 INTRODUCTION

The study of acoustic wave propagation in composite porous saturated media is a subject of interest in different fields such as geophysics, rock physics, material science, ocean acoustics¹⁻⁶ and food technology.⁷ In particular, the knowledge of the spatial distribution of ice content in permafrost areas is very important in site investigations because of its influence on the mechanical behavior of frozen soils and rocks. Also, it is useful for the detection and evaluation of gas-hydrate concentrations in ocean-bottom sediments from seismic data.^{3,8,9}

In the context of rock physics, it has been observed that the heterogeneous nature of porous rocks often results in the heterogeneity of fluid-ice distribution on scales greater than the pore sizes. While the analysis of the seismic and acoustic response associated to homogeneous or layered composite (multiphase) rocks has been studied by different authors,^{6,10,11} the influence of spatially variable petrophysical properties and unfrozen fluid and ice distributions have not received much attention yet. Some previous research related to this problem can be found in.¹² With this motivation, we developed a numerical model to investigate the effects of such heterogeneities in all the compressional and shear wave modes propagating in these media.

The behavior of the medium is described with a generalized Biot-type model recently proposed by some of the authors,^{10,11} for a porous matrix composed of two weakly coupled solids saturated by a viscous fluid. The model, stated in the space-frequency domain, includes solid matrix dissipation using a linear viscoelastic model and frequency dependent mass and viscous coupling coefficients. The heterogeneities in ice-water content at different scales are modeled using stochastic fractals.

Since the numerical simulation of waves in this kind of media is computationally expensive, due to the large number of degrees of freedom needed to calculate wave fields accurately, the use of a domain decomposition iteration is a convenient approach to overcome this difficulty. The domain decomposition procedure used in the present work was presented in¹³ for solving second-order elliptic problems and recently in^{11,14} for this particular problem. For the spatial discretization the algorithm employs the nonconforming rectangular element defined in¹⁵ to approximate the displacement vector in the solid phases. The displacement in the fluid phase is approximated by using the vector part of the Raviart-Thomas-Nedelec mixed finite element space of zero order, which is a conforming space.^{16,17}

This numerical procedure is used to obtain numerical results (snapshots and seismograms) in a real partially frozen sandstone at high frequencies, in order to analyze the correlation between the patterns of the acoustic energy associated to the different waves and the location and size of the heterogeneities, where important scattering and mode conversion effects are shown to take place.

2 GENERAL DESCRIPTION OF THE MODEL

Here we briefly review the generalities of the model to describe the static and dynamic deformation and propagation of waves in a poroelastic domain Ω consisting of a matrix composed of two different solids, indicated by the indices or supraindices 1 and 3, saturated by a single phase fluid, denoted by the index or supraindex 2, so that

$$\Omega = \Omega_1 \cup \Omega_2 \cup \Omega_3.$$

It must be emphasized that we refer the reader to papers^{10,11} to find the complete details of the formulation and the computation of the numerous coefficients involved, which for brevity will not be given in this work.

Let V_i denote the volume of the i -phase and V_b and V_{sm} the bulk volume and the solid matrix volumes, respectively, so that

$$V_{sm} = V_1 + V_3, \quad V_b = V_1 + V_2 + V_3.$$

Let us define the *bulk volumetric fractions* of the different components in the form:

$$\phi = \frac{V_2}{V_b}, \quad \phi_1 = \frac{V_1}{V_b}, \quad \phi_3 = \frac{V_3}{V_b}, \quad (1)$$

and let us introduce the solid fractions of the composite matrix

$$S_1 = \frac{V_1}{V_{sm}}, \quad S_3 = \frac{V_3}{V_{sm}}, \quad \text{with } S_1 + S_3 = 1. \quad (2)$$

The *absolute or effective porosity* of the medium is given by the ratio of the volume of the interconnected pores V_p and the total volume of the sample, i.e.,

$$\phi_a = \frac{V_p}{V_b}. \quad (3)$$

Since the present work deals with the case of a sandstone or soil at very low temperature, it is reasonable to consider that a part of the fluid which saturates the pore space is at a liquid state and the rest is frozen. Then for a given porosity ϕ_a and *bulk water content* ϕ , the following relations can be found:

$$\phi_1 = 1 - \phi_a, \quad \phi_3 = \phi_a - \phi, \quad S_3 = \frac{\phi_3}{1 - \phi}. \quad (4)$$

We will also refer to the *ice content in the pores* S'_3 , given by

$$S'_3 = \frac{V_3}{V_p} = \frac{\phi_3}{1 - \phi_1}. \quad (5)$$

One fundamental assumption in our formulation is that the two solids are non-welded (or weakly coupled), which means that they can move independently. Consequently, we can distinguish three different particle displacement fields for this model denoted by $u^{(1)}$, $u^{(2)}$ and $u^{(3)}$, representing the averaged absolute solid and fluid displacements over the bulk material Ω . We also define the relative flow of the fluid phase respect to an *effective* displacement of the composite solid matrix in the form

$$w = \phi(u^{(2)} - S_1 u^{(1)} - S_3 u^{(3)}). \quad (6)$$

As explained in¹⁰ the change in fluid content is given by

$$\zeta = -\nabla \cdot w. \quad (7)$$

Next we introduce the local stress tensors $\sigma_{ij}^{(1)}$ and $\sigma_{ij}^{(3)}$ in Ω_1 and Ω_3 , averaged over the bulk material and the fluid pressure p_f . Also, following¹⁰ we define the second order total stress tensors in Ω_1 and Ω_3 in the form

$$\sigma^{(1,T)} = \sigma_{ij}^{(1)} - S_1 \phi p_f \delta_{ij}, \quad \sigma^{(3,T)} = \sigma_{ij}^{(3)} - S_3 \phi p_f \delta_{ij}. \quad (8)$$

Let $\hat{f}(\omega)$ denote the time-Fourier transform of $f(t)$, with ω being the angular frequency and set $\hat{u} = (\hat{u}_1, \hat{w}, \hat{u}_3)$. Then the constitutive equations in the space-frequency domain are¹⁰

$$\hat{\sigma}_{ij}^{(1,T)}(\hat{u}) = [\lambda_1 \hat{\theta}_1 - B_1 \hat{\zeta} + B_3 \hat{\theta}_3] \delta_{ij} + 2\mu_1 \hat{\epsilon}_{ij}^{(1)} + \mu_{1,3} \hat{\epsilon}_{ij}^{(3)}, \quad (9)$$

$$\hat{\sigma}_{ij}^{(3,T)}(\hat{u}) = [\lambda_3 \hat{\theta}_3 - B_2 \hat{\zeta} + B_3 \hat{\theta}_1] \delta_{ij} + 2\mu_3 \hat{\epsilon}_{ij}^{(3)} + \mu_{1,3} \hat{\epsilon}_{ij}^{(1)}, \quad (10)$$

$$\hat{p}_f(\hat{u}) = -B_1 \hat{\theta}_1 - B_2 \hat{\theta}_3 + K_{av} \hat{\zeta}. \quad (11)$$

where $\hat{\epsilon}_{ij}^{(m)} = \epsilon_{ij}(\hat{u}^{(m)})$, $m = 1, 3$, is the Fourier transform of the strain tensor with linear invariant $\hat{\theta}_m$. The moduli in (9)-(11) may be complex and frequency dependent. They can be determined in terms of the properties of the individual solid and fluid phases, as explained in.¹¹

Next let the second order differential operator $\mathcal{L}(\hat{u})$ be defined by

$$\mathcal{L}(\hat{u}) = \left\{ \nabla \cdot \hat{\sigma}_{ij}^{(1,T)}(\hat{u}), -\nabla \hat{p}_f(\hat{u}), \nabla \cdot \hat{\sigma}_{ij}^{(3,T)}(\hat{u}) \right\}.$$

Then the equations of motion in a domain Ω can be written in the form¹⁰

$$-\omega^2 \mathcal{P} \hat{u} + i\omega \mathcal{B} \hat{u} - \mathcal{L}(\hat{u}) = \hat{S}(\mathbf{x}, \omega), \quad (\mathbf{x}, \omega) \in \Omega \times (0, \omega^*), \quad (12)$$

where $\mathcal{P} = \mathcal{P}(\omega) \in \mathbf{R}^{9 \times 9}$ is a positive definite mass matrix and $\mathcal{B} = \mathcal{B}(\omega) \in \mathbf{R}^{9 \times 9}$ is a nonnegative dissipation matrix whose coefficients are defined in.¹¹ Also,

$$S(\mathbf{x}, \omega) = (S^1(\mathbf{x}, \omega), S^f(\mathbf{x}, \omega), S^3(\mathbf{x}, \omega))$$

denotes the external source, \mathbf{x} the position and ω^* is an upper temporal frequency of interest.

Using a variational formulation of the problem (12) with an absorbing boundary condition, the iterative domain decomposition procedure is defined in a two-dimensional rectangular domain Ω in the (x, z) plane as described in.¹¹ The choice of the nonconforming element used to compute the solid displacement is based on the dispersion analysis performed in¹⁸ showing that it almost halves the number of points per wavelength needed to reach a desired accuracy as compared with the standard conforming bilinear element. The space–time solution is obtained by solving the variational formulation of (12) for a finite number of frequencies and using an approximate inverse Fourier transform.¹⁹

From a theoretical plane wave analysis we found for this model that three different compressional waves (P1, P2 and P3) and two shear waves (S1, S2) can propagate¹⁰ in agreement with.¹ The P1 and S1 waves correspond to the classical fast longitudinal and transversal waves propagating in elastic or viscoelastic isotropic solids. The additional slow modes are waves strongly attenuated in the low frequency range, related to motions out of phase of the different phases. The experimental observation of the slow waves in this kind of media was reported by Leclaire et al.²⁰

3 THE NUMERICAL EXPERIMENT

To show the implementation of the numerical procedure we perform a numerical experiment in a sample of water saturated partially frozen sandstone with a spatially variable ice - water content distribution in the pores. Our aim is to obtain snapshots and traces of the particle velocity fields in the different phases. We also performed a simulation for a homogeneous case for a better interpretation of the results.

3.1 Construction of the heterogeneous ice - water distribution model

For this experiment we consider a sandstone with absolute porosity $\phi_a = .18$, with a spatially variable bulk water content distribution ϕ chosen so that the ice content S'_3 in most of the pores equals 0.2 (i.e. $\phi = 0.144$), while in other zones there exist irregular *patches* of high ice content equal to 0.7 ($\phi = 0.054$).

The generation of this distribution requires several steps, and involves the use of a stochastic fractal field, based on the so-called von Karman self-similar correlation functions. These models are widely used in the statistical characterization of heterogeneities for different applications. Following^{21,22} and more recently,²³ we consider a particular case for which the spectral density is given by:

$$S_d(k_x, k_z) = S_0(1 + k^2 a^2)^{-(H+E/2)} \quad (13)$$

where $k = \sqrt{k_x^2 + k_z^2}$ is the radial wavenumber, a the correlation length, H is a self-similarity coefficient ($0 < H < 1$), S_0 is a normalization constant and E is the Euclidean dimension. Equation (13) corresponds to a fractal process of dimension $D = E + 1 - H$ at scales smaller

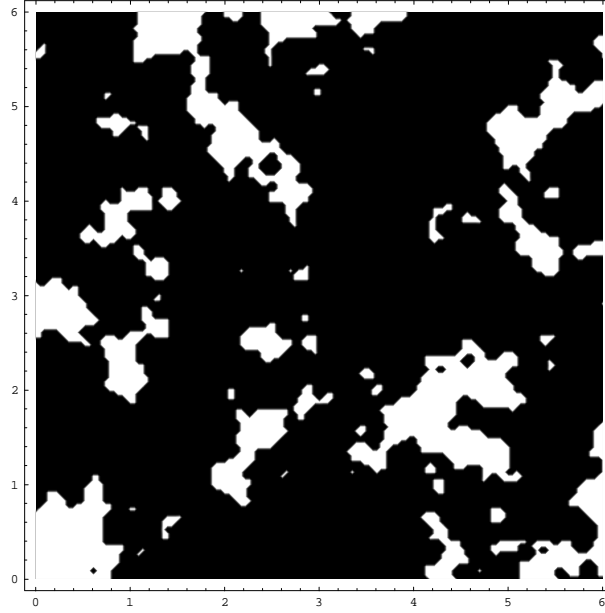


Figure 1: Heterogeneous water-ice content distribution within the computational domain. The black (resp. white) zones correspond to 80 % water - 20 % ice; $\phi = 0.144$ (resp. 30 % water - 70 % ice; $\phi = 0.054$) in the pores.

than a . For this application we take $E=2$, $a=0.3$ cm and $D=2.2$. The first step was to assign to each point of the mesh a pseudo-random number using a generator with uniform distribution (white noise). This field was then Fourier transformed to the spatial wavenumber domain and its amplitude spectrum was then filtered using (13). The result was then transformed back to the spatial domain, forced to have zero mean and normalized to the range, (0.054, 0.144), obtaining a *micro-heterogeneity* model. Next, to construct the patchy distribution (i.e. the *macro-heterogeneity* model), the water content at each point of the grid was modified so that for cells having a ϕ less than a threshold level ϕ^* we changed the value to 0.054 and where $\phi > \phi^*$ we assigned a water content equal to 0.144. The result is illustrated in Figure 1.

3.2 Physical constants, wave velocities and attenuation coefficients

The material properties of the system, taken from Refs.^{3,12} are given in Table 1. In this case the indexes 1, 2 and 3 correspond to the sandstone, water and ice, respectively. The computation of the elastic coefficients requires some values for the bulk and shear modulus of the two solid (dry) frames, denoted by $K_{s1,m}$, $K_{s3,m}$, $\mu_{s1,m}$ and $\mu_{s3,m}$, respectively.¹¹ Following Refs.^{1,3} and¹⁰ it is assumed that $K_{s1,m} = 14.4$ GPa and that the moduli $\mu_{s1,m}$, $\mu_{s3,m}$ and $K_{s3,m}$ can be computed by means of a percolation-type model using the relations and the same constants given in¹¹ for the parameters K_{s1} , μ_{s1} , K_{s3} , μ_{s3} and K_a , μ_a , shown in Table 1.

To introduce viscoelasticity in the formulation we replaced the real poroelastic coefficients in the constitutive relations (9)-(11) by complex frequency dependent poroviscoelastic moduli. For this purpose we use the linear viscoelastic model presented by²⁴ with parameters chosen so that the quality factors associated to each modulus are almost constant in the frequency range

were the equations are solved (see¹¹).

The mass and dissipative coefficients in matrices \mathcal{P} and \mathcal{B} are computed using the formulae in¹¹ with the constants given in Table 1. The formulation is valid for the full frequency range since it includes frequency dependent viscodynamic interaction among the two solids and the fluid.

Solid grain	bulk modulus, K_{s1} shear modulus, μ_{s1} density, ρ_1 permeability $\kappa_{1,0}$	38.7 GPa 39.6 GPa 2650 kg/m ³ 1.07 10 ⁻¹³ m ²
Ice	bulk modulus, K_{s3} shear modulus, μ_{s3} density, ρ_3 permeability $\kappa_{3,0}$	8.58 GPa 3.32 GPa 920 kg/m ³ 5 10 ⁻⁴ m ²
Fluid	bulk modulus, K_f density, ρ_2 viscosity, η	2.25 GPa 1000 kg/m ³ 1.798 cP
Air	bulk modulus, K_a shear modulus, μ_a	1.5 10 ⁻⁴ GPa 0 GPa

Table 1. Material properties of the frozen sandstone model.

Wave	Ice content in the pores 0.2		Ice content 0.7	
	phase vel. (Km/s)	attenuation (dB)	phase vel. (Km/s)	attenuation (dB)
Fast P1 wave (Vp1)	3.98	0.08	4.38	0.062
Slow P2 wave (Vp2)	0.78	6.48	1.40	3.956
Slow P3 wave (Vp3)	0.12	3.18	0.19	19.2
Fast S1 wave (Vs1)	2.39	0.24	2.72	0.23
Slow S2 wave (Vs2)	0.10	0.39	0.59	2.22

Table 2. Wave speeds and attenuation factors for all waves at frequency 500 kHz.

In Table 2 we display the phase velocities and attenuation factors (in dB) at 500 kHz for the five different types of waves, for the low and high ice concentration levels used in the experiment. This shows the important velocity and attenuation contrasts between the “black” and “white” zones in Figure 1 and also the different behaviour of the waves for a given frequency. We also plot in Figure 2 the variation of phase velocities versus ice content in the pores.

3.3 Mesh, source and receiver geometry

The computational domain Ω is a square of side length $L = 5$ cm, with a uniform partition in the plane (x, z) into squares of side length $h = L/N_x$, with $N_x = N_z = 276$, resulting $h = 0.018$

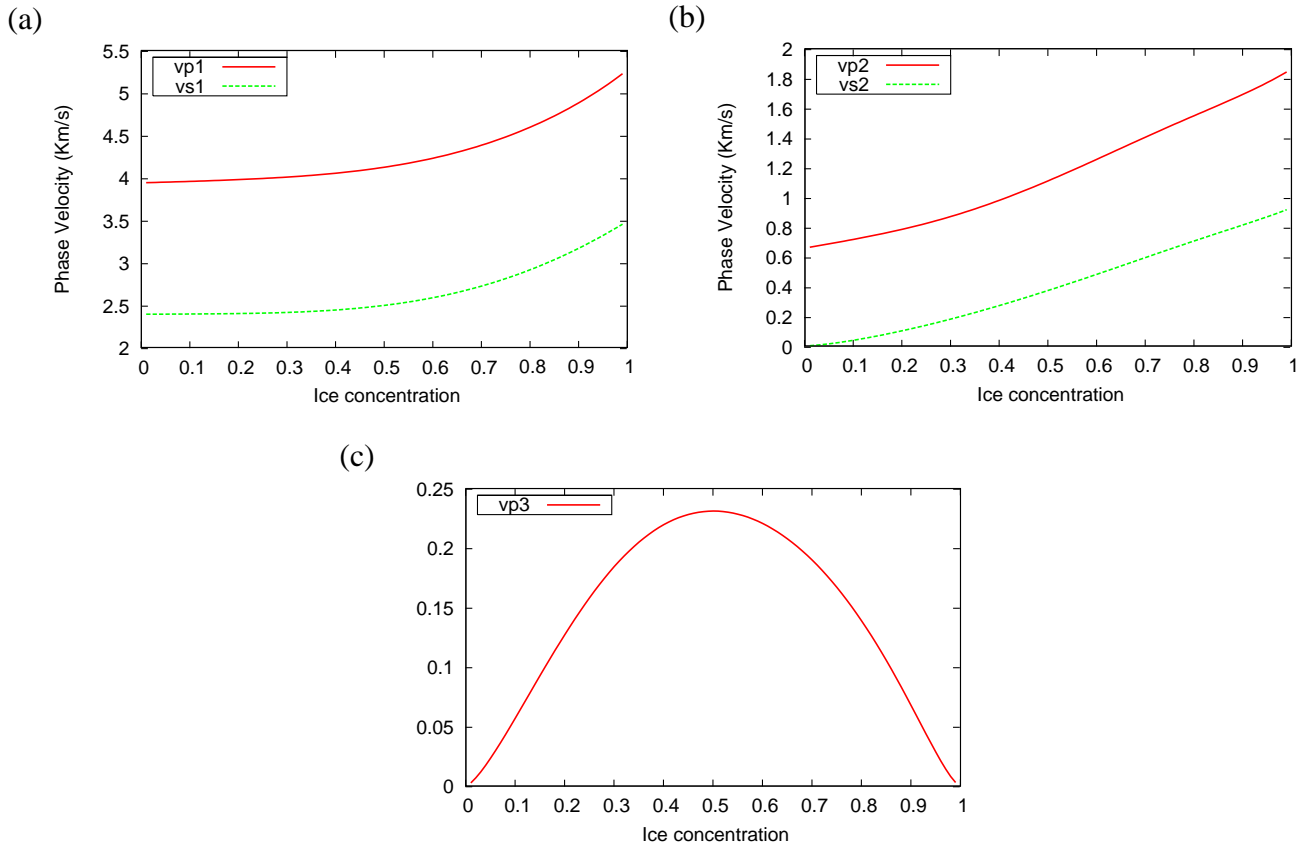


Figure 2: Phase velocities versus ice content in the pores for a frequency $\omega=500$ kHz.

cm. This configuration was designed taking into account the limitations in the available memory size and simulation time. With this mesh size the resulting number of points per wavelength at the central frequency is about 42 for the fast P1 wave and about 2 for the slow waves.

The oscillatory source function (S^1, S^f, S^3) in (12) is a compressional and shear point source of ultrasonic waves located at $(x_s, z_s) = (2.5 \text{ cm}, 4.0 \text{ cm})$, applied to the bulk volume, with a band limited spectrum of central frequency $f_0 = 500$ kHz. Its time dependence $s(t)$ is given by:

$$s(t) = -2\xi(t - t_0)e^{-\xi(t-t_0)^2}, \quad (14)$$

with $\xi = 8f_0^2$ and $t_0 = 1.25/f_0$. The spectrum of $\hat{s}(\omega)$ is negligible for frequencies $\omega > 2\pi 1000$ kHz. We also located a receiver at position $(x_r, z_r) = (3.5 \text{ cm}, 1.5 \text{ cm})$ to record traces of the z-component and divergence of the particle velocity for each solid and fluid phase. The numerical problem was solved for 110 equally spaced temporal frequencies in the interval $(0, 1 \text{ mHz})$ for a simulation time of 0.08 msec. The total CPU time was about 113 hours in a serial SUN Workstation machine. The parallelization of the domain decomposition algorithm is currently being implemented.

4 ANALYSIS OF RESULTS AND CONCLUSIONS

The following set of figures present the snapshots obtained for this experiment. To understand and identify more clearly the various kinds of waves propagating in the computational domain we also computed the corresponding curl and divergence of the different fields. For brevity, among the whole set of snapshots obtained for the solid and fluid phases during the simulation time, we only show those corresponding to solid 1, at three different times.

Figures 3(a)-(b) show respectively snapshots of the vertical component and the divergence of the particle velocity of the solid phase 1 at $t = 0.0045$ ms, where we can observe the propagation of the two direct fast waves P_1 and S_1 , and the initial development of the slow P_2 direct wave front around the source. Note the generation of secondary fast compressional waves to the right of the source, associated to the presence of the high ice content patch.

The next figures (Figure 4 (a)-(b)) show the evolution of the different wavefronts at a time $t = 0.0065$ ms, where the presence of heterogeneities in the ice - water content distribution distant of the source can be clearly correlated with the patterns of wave propagation.

Some time later, at $t = 0.05$ ms, after the direct fast waves escaped from the domain, we observe in Figure 5 (a)-(b) the presence of many “sources” of slow P_2 waves (note their short wavelengths), whose location show a very strong correlation with the distribution of the patches of higher ice content. These waves are associated to wave mode conversion phenomena that take place when the fast waves propagate through the heterogeneities of the domain. Scattering and interference effects are also observed in the picture, showing the complex character of wave phenomena in this kind of media.

Finally, in Figure 6 (a)-(b) we plot traces of the vertical component and the divergence of the particle velocity of the solid phase 1 versus simulation time at the fixed receiver position (x_r, z_r) . We compare the results for the heterogeneous model with those obtained for an homogeneous distribution of water content, with a constant value equal to $\phi = 0.144$ (i.e. the value corresponding to the dark zones in Figure 1). For the homogeneous case it is possible to identify the P_1 , S_1 and the slow wave P_2 . The other two slow wave modes are not visible in the simulation, due not only to their very low velocities and high attenuation (see Table 2) but also to the limitations imposed by the mesh size.

As a conclusion we can state that the results presented in this work show that the numerical model allows for a correct simulation of wave propagation in highly heterogeneous composite porous media. Moreover, the solution of this modeling problem may be useful as a first step in the analysis and further development of indicators to quantify the presence, distribution, characteristic size and concentration of ice-water, or equivalently, clay distributions in real reservoir rocks and partially frozen soils.

ACKNOWLEDGEMENTS

This work was partially funded by the Agencia Nacional de Promoción Científica y Tecnológica (PICT03 3-13376) and CONICET (PIP05-06 5126).

REFERENCES

- [1] Ph. Leclaire, F. Cohen-Tenoudji, and J. Aguirre Puente. Extension of Biot's theory of wave propagation to frozen porous media. *J. Acoust. Soc. Amer.*, **96** (6), 3753–3767 (1994).
- [2] J. M. Carcione, B. Gurevich, and F. Cavallini. A generalized Biot-Gassmann model for the acoustic properties of shaley sandstones. *Geophysical Prospecting*, **48**, 539–557 (2000).
- [3] J. M. Carcione and U. Tinivella. Bottom-simulating reflectors: Seismic velocities and AVO effects. *Geophysics*, **65** (1), 54–67 (2000).
- [4] J. L. Morack and J. C. Rogers. Seismic evidence of shallow permafrost beneath the islands in the Beafort Sea. *Arctic*, **3**, 166–174 (1981).
- [5] J. M. Carcione and G. Seriani. Seismic velocities in permafrost. *Geophysical Prospecting*, **46**, 441–454 (1998).
- [6] J. M. Carcione and G. Seriani. Wave simulation in frozen porous media. *J. Computational Physics*, **170**, 676–695 (2001).
- [7] S. Lee, P. Cornillon, and O. Campanella. Propagation of ultrasound waves through frozen foods. *Proceedings of the 2002 Annual Meeting and Food Expo., Anaheim (CA)*, (2002).
- [8] J. M. Carcione and D. Gei. Gas-hydrate concentration estimated from p- and s-wave velocities at the Mallik 2L-38 research well, Mackenzie Delta, Canada. *J. of Applied Geophysics*, **56**, 73 – 78 (2004).
- [9] S. Chand and T. A. Minshull. Seismic constraints on the effects of gas-hydrate on sediment physical properties and fluid flow:a review. *Geofluids*, **3**, 275 – 289 (2003).
- [10] J. E. Santos, C. L. Ravazzoli, and J. M. Carcione. A model for wave propagation in a composite solid matrix saturated by a single-phase fluid. *J. Acoust. Soc. Am.*, **115**(6), 2749–2760 (2004).
- [11] C. L. Ravazzoli and J. E. Santos. A domain decomposition procedure for the simulation of waves in fluid saturated composite poroviscoelastic media. *Mecánica Computacional*, **23**, 3191–3209 (2004).
- [12] J.M. Carcione, J. E. Santos, C. L. Ravazzoli, and H. B. Helle. Wave simulation in partially frozen porous media with fractal freezing conditions. *J. Appl. Physics*, **94**, 7839–7847 (2003).
- [13] J. Douglas Jr, P. L. Paes Leme, J. E. Roberts, and J. Wang. A parallel iterative procedure applicable to the approximate solution of second order partial differential equations by mixed finite element methods. *Numer. Math.*, **65**, 95–108 (1993).
- [14] J. E. Santos and D. Sheen. Finite element methods for the simulation of waves in composite saturated poroviscoelastic materials. *SIAM J. Numer. Anal.* (submitted), (2005).

- [15] J. Douglas Jr., J. E. Santos, D. Sheen, and X. Ye. Nonconforming Galerkin methods based on quadrilateral elements for second order elliptic problems. *RAIRO Math. Modeling and Numer. Analysis (M2AN)*, **33**, 747–770 (1999).
- [16] P. A. Raviart and J. M. Thomas. Mixed finite element method for 2nd order elliptic problems. *Mathematical Aspects of the Finite Element Methods, Lecture Notes of Mathematics, vol. 606, Springer*, (1975).
- [17] J. C. Nedelec. Mixed finite elements in r^3 . *Numer. Math.*, **35**, 315–341 (1980).
- [18] F. I. Zyserman, P. M. Gauzellino, and J. E. Santos. Dispersion analysis of a non-conforming finite element method for the helmholtz and elastodynamic equations. *Int. J. Numer. Meth. Eng.*, **58**, 1381–1395 (2003).
- [19] J. Douglas Jr., J. E. Santos, D. Sheen, and L. Bennethum. Frequency domain treatment of one-dimensional scalar waves. *Math. Models Methods Appl. Sci.*, **3**, 171–194 (1993).
- [20] Ph. Leclaire, F. Cohen-Tenoudji, and J. Aguirre Puente. Observation of two longitudinal and two transverse waves in a frozen porous medium. *J. Acoust. Soc. Amer.*, **97**, 2052–2055 (1995).
- [21] A. Frankel and R. W. Clayton. Finite difference simulation of seismic wave scattering: implications for the propagation of short period seismic waves in the crust and models of crustal heterogeneity. *J. Geophys. Res.*, **91**, 6465–6489 (1986).
- [22] N. H. Pham H.B. Helle and J.M. Carcione. Velocity and attenuation in partially saturated rocks - poroelastic numerical experiments. *Geophysical Prospecting*, **51**, 551–566 (2003).
- [23] P.M. Gauzellino J.E. Santos, C.L. Ravazzoli and J.M.Carcione. Numerical simulation of ultrasonic waves in reservoir rocks with patchy saturation and fractal petrophysical properties. *Computational Geosciences*, **9**, 1–27 (2005).
- [24] H. P. Liu, D. L. Anderson, and H. Kanamori. Velocity dispersion due to anelasticity; implications for seismology and mantle composition. *Geophys. J. R. Astr. Soc.*, **147**, 41–58 (1976).

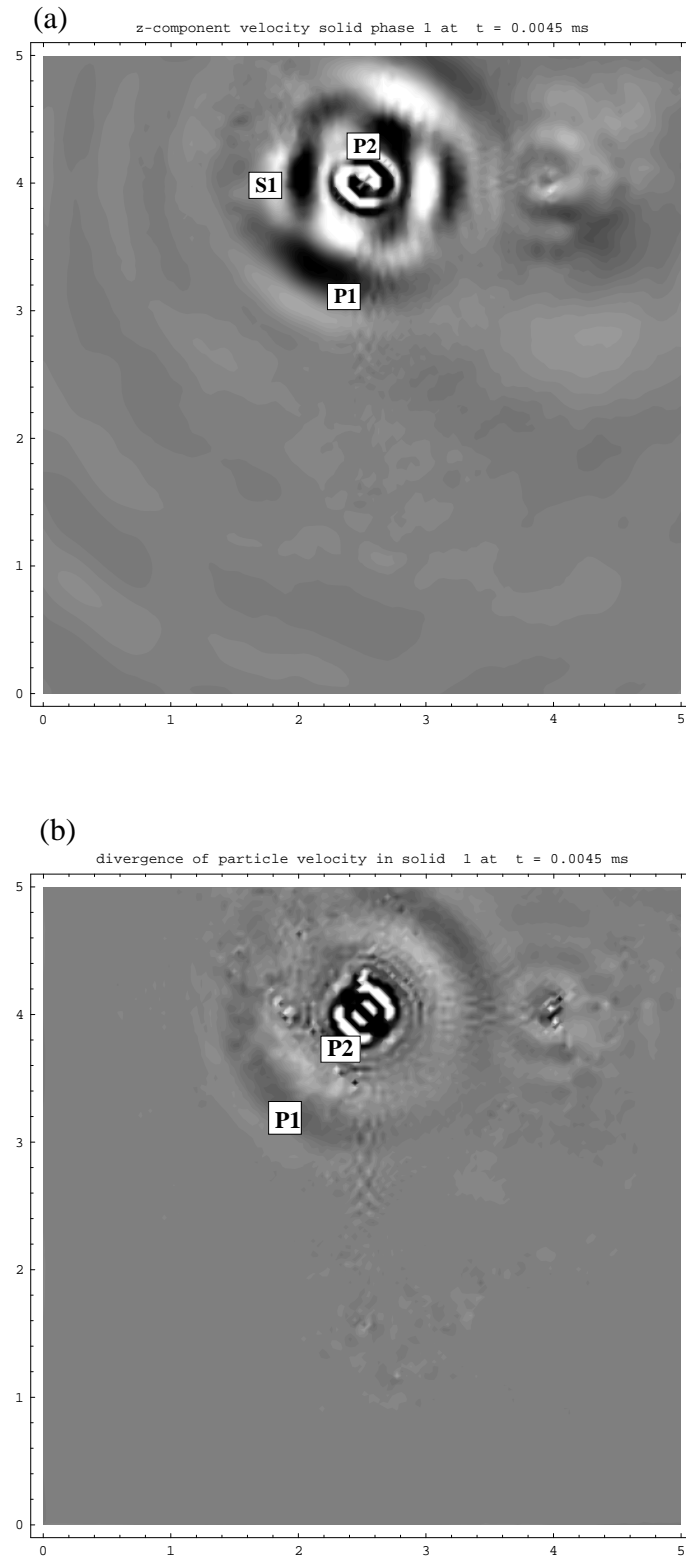


Figure 3: Snapshots of the vertical component of the particle velocity field (a) and its divergence (b) at $t = 0.0045$ ms for the solid phase 1.

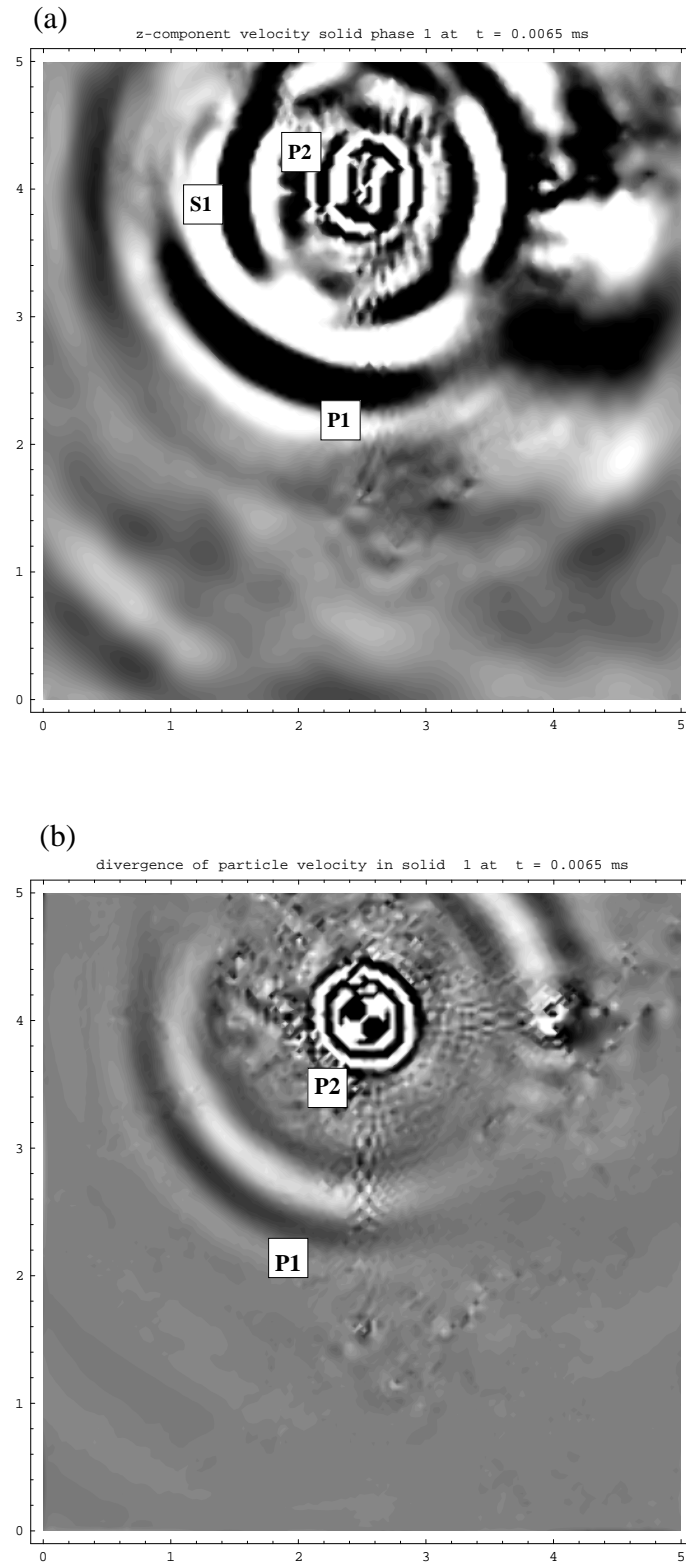


Figure 4: Snapshots of the vertical component of the particle velocity field (a) and its divergence (b) at $t = 0.0065$ ms for the solid phase 1.

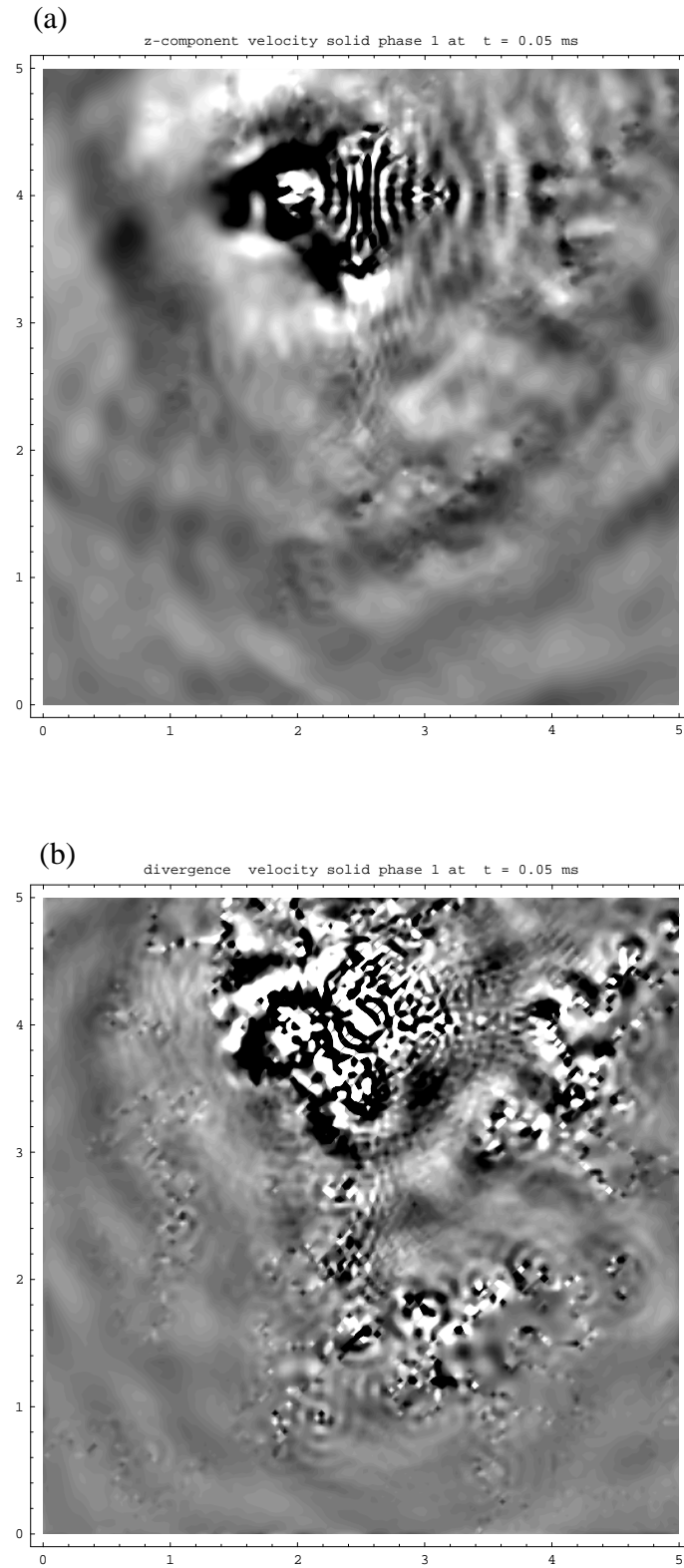


Figure 5: Snapshots of the vertical component of the particle velocity field (a) and its divergence (b) at $t = 0.05$ ms for the solid phase 1.

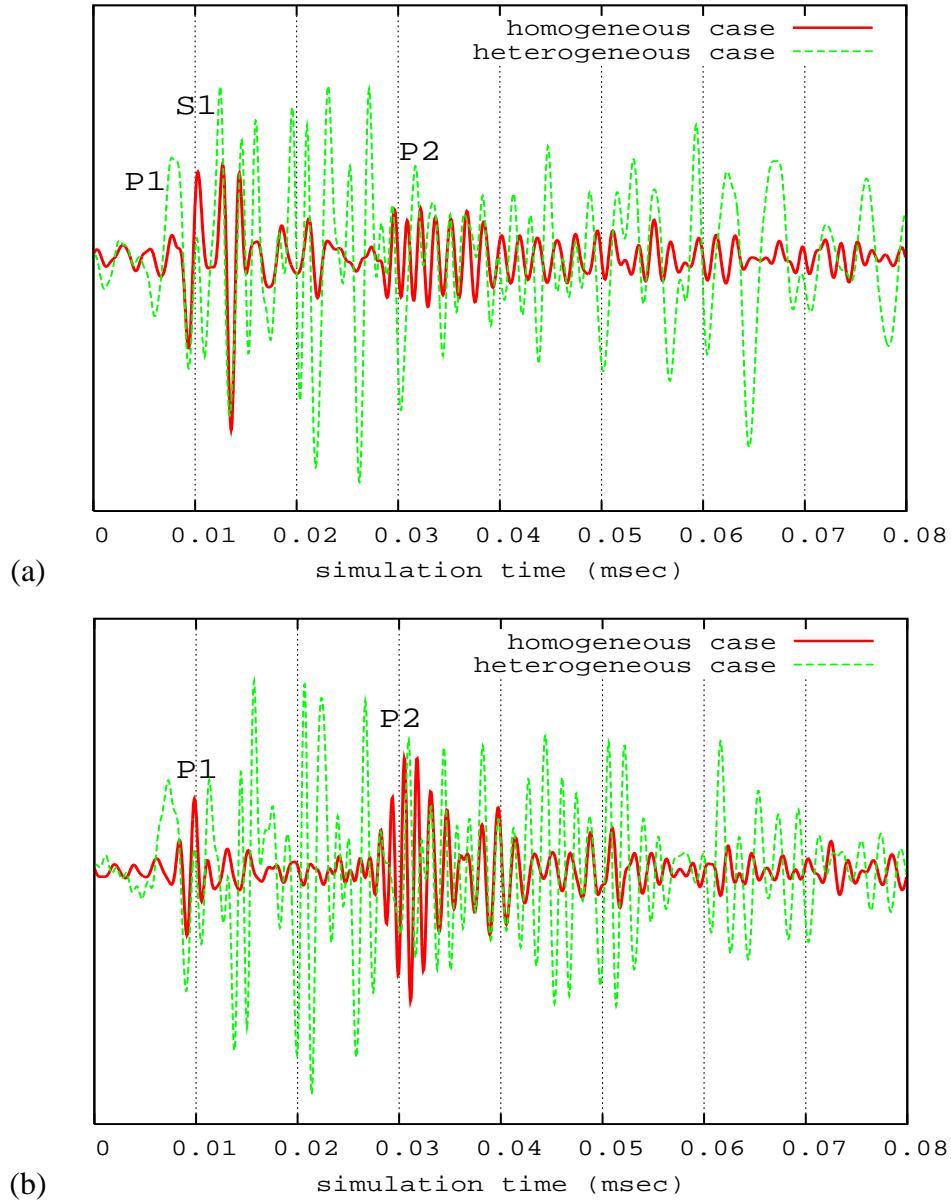


Figure 6: Traces at a receiver located at coordinates $(x_r, z_r) = (3.5 \text{ cm}, 1.5 \text{ cm})$ showing in (a) the vertical component, and in (b) the divergence of the particle velocity field of the solid phase 1.